Additive Manufacturing Letters 15 (2025) 100331

Contents lists available at ScienceDirect

Additive Manufacturing Letters

journal homepage: www.elsevier.com/locate/addlet

Short Communication

Effect of interface orientation in laser powder bed fusion of IN718/GRCop-42 bimetallic parts for Aerospace

Alasdair Bulloch [a,*], Amanda Cruchley [b], Allin Groom [c], Andy Harris [c], Fiona Schulz [b], Christopher J. Tuck [a], Richard Hague [a], Marco Simonelli [a]

[a] Centre for Additive Manufacturing, University of Nottingham, Nottingham NG8 1BB, UK
[b] The Manufacturing Technology Centre, Ansty Park, Coventry CV7 9JU, UK
[c] Autodesk Research, Autodesk Ltd., 6 Agar Street, London WC2N 4HN, UK

ARTICLE INFO

Keywords:
Multi-material additive manufacturing
Laser powder bed fusion
Interface orientation
GRCop-42
Combustion chamber

ABSTRACT

Additive manufacturing of bimetallic parts has gathered significant interest in recent years. Of particular relevance is the combination of Ni-based superalloys and Cu-based alloys suitable for high temperature applications, such as those found in aerospace rocket engines. To provide confidence in the production of such bimetallic parts, a detailed understanding of the process-structure relationship is required. This study investigates the effect of deposition sequence and recoating direction on the interfacial microstructure evolution in samples where material is graded through horizontal, vertical and angled interfaces. The samples in this study are produced through laser powder bed fusion of IN718 and GRCop-42, using a Schaeffler Aerosint selective powder deposition recoater. Analysis was conducted through a combination of backscatter electron imaging, x-ray diffraction, energy dispersive spectroscopy, and electron backscatter diffraction. For a horizontal interface, the deposition sequence has a significant effect on the presence of defects and phase formation at the interface. The recoating direction is shown to have an influence on the mixing behaviour for vertical and angled interfaces, with a gradual transition of the alloys produced when the interface is aligned parallel to the recoating direction. In contrast either a significant crossing of the first-deposited material across the interface occurs, or a sudden change in composition develops when deposition is perpendicular to the interface. On the basis of these findings, design rules can be developed to ensure the fabrication of suitably designed bimetallic parts for high temperature applications such as rocket engines in the aerospace sector.

1. Introduction

Through the layer-wise approach to combining dissimilar alloys, multi-metal additive manufacturing (AM) enables the fabrication of high-performance components with spatially tailored properties [1,2]. This is particularly valuable for aerospace applications, such as regeneratively cooled combustion chambers, which demand materials offering high-temperature strength and high thermal conductivity.

In such systems, it is common to pair a nickel-based superalloy with a copper alloy [3–5]. The structural jacket of the combustion chamber is often fabricated from IN718, due to its exceptional strength and corrosion resistance at high temperatures [6]. GRCop-42, a CuCrNb ternary alloy, was developed by NASA and is used as the internal wall lining to increase heat dissipation [7]. The Cr and Nb content predominantly precipitate as a Cr_2Nb Laves phase. This allows for the matrix of the alloy to be close to pure Cu, providing the alloy with exceptional thermal and electrical conductivity properties [8]. The high thermal stability of the Cr_2Nb phase strengthens the alloy at high temperatures [8,9], and reduces the thermal expansion (relative to pure Cu). Based on this, the use of GRCop-42 instead of pure copper is expected to reduce thermally induced stresses at the interface (with the structural jacket) during thermal cycling in service [10].

The line-by-line, layer-wise nature of AM enables tailoring of the interfacial geometry between dissimilar materials, which is difficult with conventional joining (e.g., welding, diffusion bonding). In particular, the high resolution processing of laser powder bed fusion (PBF-LB) [2], allows for complex interface geometries that can enhance bond integrity [11].

Several approaches exist to produce multi-material parts by PBF-LB. In many systems, a single material is first deposited and selectively laser-

* Corresponding author.
E-mail address: alasdair.bulloch@nottingham.ac.uk (A. Bulloch).

https://doi.org/10.1016/j.addlet.2025.100331
Received 6 June 2025; Received in revised form 29 September 2025; Accepted 11 October 2025
Available online 12 October 2025

melted, with the unmelted powder then removed using a vacuum [12] or a flexible scraping blade [11]. Following this, a second material is added by spreading from a secondary hopper [13] or depositing from a nozzle [14]. These methods require multiple recoating actions per layer of the build and therefore have a slow build rate [1]. On the other hand, the three material selective powder deposition (SPD) recoater developed by Schaeffler Aerosint deposits multiple powders in a single recoating action, allowing for a build rate closer to that of single material PBF-LB.

As individual alloys, both IN718 [15,16] and GRCop-42 [10,17,18] have been successfully fabricated using PBF-LB and directed energy deposition (DED). Subsequently, these two alloys (or similar Ni and Cu-based alloys) have been combined for bimetallic applications [3,4,11,19–21], with several outlining the improvement in thermal diffusivity [19,21], absence of cracking [3,11], and good interfacial strength [11,20,21], as well as detailed studies of the interface microstructure [3,4,11,19,21], and the presence of lack of fusion (LoF) when depositing IN718 on GRCop-42 [3].

However, these studies have focussed primarily on planar interfaces aligned parallel to the build direction (BD). Whereas multi-material AM components will feature interface planes which may be perpendicular to the BD, or at an angle in between, depending on the part geometry and build orientation. Changes to the orientation of the interface plane will affect the direction of heat loss and subsequently alter the thermal history. Additionally, due to the method of multi-material deposition, the interface orientation can affect how each alloy is distributed across the interface.

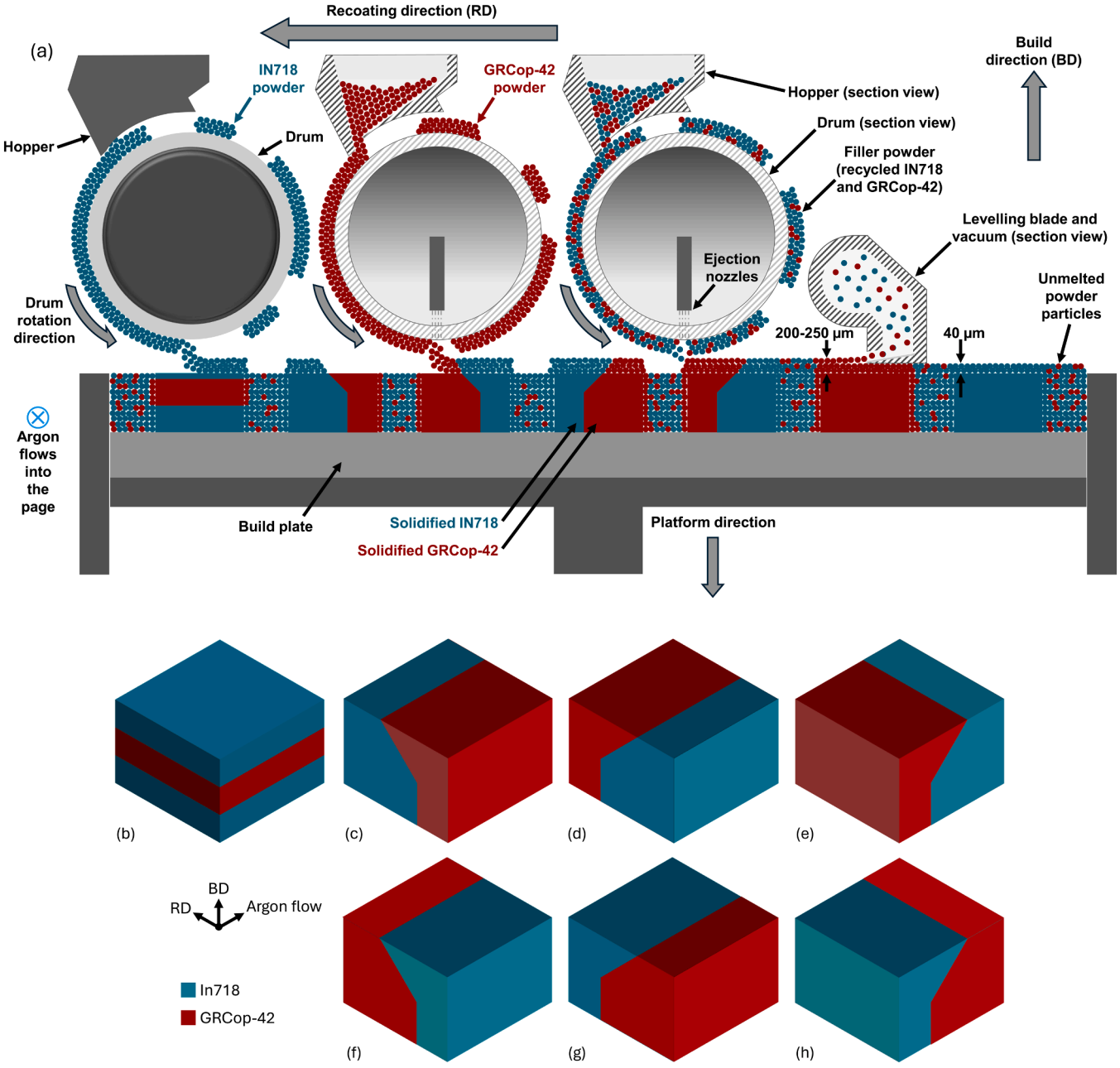

Fig. 1. (a) Schematic of the Schaeffler Aerosint SPD recoater used to deposit three distinct metal powders – IN718, GRCop-42, and a filler material – in a single pass over the substrate. This schematic is adapted from our previous work [22], licensed under CC BY 4.0 (http://creativecommons.org/licenses/by/4.0/). Changes were made to the original to reflect the current material system and powder arrangement. The device recoats from the left to the right, with all drums rotating counterclockwise. Argon flows into the page. (b-h) Schematics of the samples produced for this study. Due to the order of the drums and recoating direction, within the same layer, IN718 is deposited before GRCop-42 with the filler powder following GRCop-42.

It is critical to evaluate these effects on the microstructure evolution to provide confidence in the operation of such bimetallic structures. This study investigates how both interface orientation (horizontal, vertical, and 45° angled incline) and recoating direction (RD) influence element mixing, microstructure evolution, and defect formation at the interface of IN718 and GRCop-42. A three material selective powder deposition (SPD) recoater developed by Schaeffler Aerosint is used to produce the bimetallic parts of IN718 and GRCop-42. This knowledge not only enables confidence in the robustness of PBF-LB produced bimetallic IN718/GRCop-42 structures, but also indicates potential guidelines for other bimetallic systems produced using PBF-LB.

2. Materials and methods

Bimetallic samples of combined IN718 and GRCop-42 were fabricated in an AconityMIDI+ PBF-LB machine (Aconity3D Gmbh, Germany), equipped with a 1 kW continuous wave ytterbium fibre laser (nLIGHT alta, USA) operating at 1070 nm wavelength and with a beam spot diameter of 80 μm. A Schaeffler Aerosint SPD recoater (Schaeffler Aerosint, Belgium) capable of simultaneously depositing up to three different powders in a single pass over the substrate, was used to enable spatially controlled multi-material deposition.

This SPD recoater uses three vacuum-regulated cylindrical drums coated with a wire mesh, which retain a layer of powder on their surfaces. Powder is released from each drum, via an arrangement of nozzles within the drum, as they pass over the substrate. A levelling blade follows to create a uniform 40 μm thick powder layer. A schematic of the deposition method is shown in Fig. 1(a), adapted from our previous work [22] under the terms of the Creative Commons Attribution 4.0 License (http://creativecommons.org/licenses/by/4.0/) and modified to reflect the new powder deposition arrangement. Powder deposition proceeds from right to left. Within each layer, IN718 is deposited first, followed by GRCop-42. A third powder (a mix of recycled powder from prior builds) is then deposited to fill in the remaining area around the build plate. Argon shielding flows into the page.

The feedstock was gas-atomised IN718 (Oerlikon Metco Europe GmbH, Germany) and GRCop-42 (Carpenter Additive, UK) powders. The composition of each was measured by the suppliers using inductively coupled plasma mass spectrometry and are provided in Table 1. The particle size distribution (PSD) for each were measured using a Mastersizer 3000 (Malvern Panalytical, UK), and the morphology of the powders were analysed using a Hitachi TM3030 secondary electron microscope (SEM) (Hitachi, Japan). A summary of these results is given in the appendix, Figure A 1. GRCop-42 powder presented near-spherical morphology with a high fraction of fine particles, both alone and satelliting to the larger particles. IN718 powder was more uniformly spherical with fewer satellites. The PSD of both powders is shown to be monomodally distributed with a PSD of D10 = 17.1 μm, D50 = 28.5 μm, and D90 = 46.2 μm, and D10 = 23.0 μm, D50 = 34.0 μm, and D90 = 50.3 μm for GRCop-42 and IN718 respectively. Virgin powder was used for all the builds in this study.

The thermophysical and elastic properties of each of the two alloys were not measured in this study, but their effects are discussed. The relevant properties are taken from existing studies (using PBF-LB) and summarised in Table 2.

Single material studies were conducted for each alloy to establish parameters to produce > 99.9 % dense parts. These parameters (highlighted in Table 3) were used for the respective alloys of the bimetallic samples.

Table 1
Measured chemical composition of GRCop-42 and IN718 powder used in this study.

Material	Element [wt %]							
	Al	Cr	Cu	Fe	Mo	Nb	Ni	Ti
GRCop-42		3.30	Bal.			2.70		
IN718	0.44	17.17		15.96	2.84	4.81	Bal.	0.90

Table 2
Thermal properties of IN718 and GRCop-42.

Alloy	Thermal conductivity ($(W{\cdot}m^{-1}K^{-1})$)		Coefficient of Thermal Expansion, CTE ($x10^{-6}K^{-1}$)	Elastic Modulus, E (GPa)
	Room temperature	Elevated temperature		
In718	11.4 [23]	26.7 (liquidus) [23]	11.9 [24]	~200 [25]
GRCop-42	330.0 [10]	295.0 (700 °C) [10]	17–18 [8,10]	~80 [18]

Sandwich structures were created for the analysis of horizontal interfaces. These structures, shown in Fig. 1(b), feature a 10 mm x 10 mm footprint and have a total height of 6 mm. The individual alloy sections are 2 mm tall in the sequence of IN718 – GRCop-42 – IN718. To analyse samples with a vertical and angled interface, cubes with a 10 mm x 10 mm footprint and 8 mm tall are manufactured with a vertical interface that leads into a 45° degree angle at 4 mm build height. To assess the effect of the RD relative to the vertical and angled interface, these samples are duplicated and rotated around the z axis (aligned to the BD), as shown by the orientation of the samples in Fig. 1(c-h). The samples with GRCop-42 on top of IN718 for the angled portion are shown in Fig. 1(c-e), for each orientation. Similarly, the samples with IN718 on top of GRCop-42 for the angled portion are shown in Fig. 1(f-h), for each orientation. The exact dimensions of these samples are shown in the appendix, Figure A 2. All bimetallic samples produced feature a step change in 100 % IN718 powder to 100 % GRCop-42 powder deposited at the interface. There was no graded transition using mixtures of the two powders.

To assess interfacial evolution with respect to build direction, a second set of IN718/GRCop-42 rectangular samples (with a horizontal interface) were created. Twenty layers of the upper material were deposited (and laser melted), such that the height at which the material deposition was changed could be estimated in post-processing. Both deposition sequences were fabricated.

All samples were produced under an argon atmosphere (with oxygen level below 500 ppm), and with a hatch rotation angle of 90° between each layer. Prior to each build, the laser-to-powder alignment was verified by laser scanning the contour of the deposited IN718. Any offset was measured and adjustments made to x and y-axis offset values.

The samples were sectioned parallel to the BD, mounted, ground, and finished with colloidal silica polishing. A Hitachi TM3030 SEM was used to capture secondary electron images for relative density analysis of the individual alloys using ImageJ (National Institutes of Health, USA). A JEOL 7100 field emission gun SEM (JEOL, Ltd., Japan) equipped with a NordlysMax3 electron backscatter diffraction (EBSD) detector and Oxford Instruments Advanced X-max 150 energy dispersive spectroscope (EDS) detector was used to capture backscatter electron images, along with chemical composition and crystallographic data of the specimens. An accelerating voltage of 15 kV and a step size of 0.35 μm was used for collecting the EBSD data.

EDS and X-ray diffraction (XRD) depth profiling were conducted on the second set of samples to investigate the interfacial composition and phase evolution. This approach enables a more complete identification of phases at the interface, as was previously shown to be critical in multi-material PBF-LB systems [22]. In this work, a similar methodology was adopted.

For EDS analysis, compositional data were recorded at 10 μm intervals along twelve evenly spaced scan lines (100 μm apart), all aligned parallel to the BD and spanning the entire interface region (shown in appendix, Figure A 3). The data was averaged to create a representative compositional profile across the interface.

Table 3
Parameters used for processing IN718 and GRCop-42 powder in this study.

Material	Laser power (W)	Scan speed (mm/s)	Hatch distance (μm)	Spot diameter (μm)	Layer thickness (μm)	Hatch rotation angle (°)	Stripe width (mm)
IN718	200	800	80	80	40	90	5
GRCop-42	340	800	100	80	40	90	5

XRD measurements were captured at 50 μm and 100 μm intervals in the BD for the deposition of IN718 on GRCop-42 and GRCop-42 on IN718 respectively. To access the correct depths, the samples were carefully ground and polished to the correct height using a set of calipers to measure the overall height of the sample removed. For example, to analyse the transition line (where the material deposited changes in the BD), the sample height was reduced by 800 μm (approximately 20 layers, as shown in Figure A 3). A step size of 0.02° and a step time of 3 s scanning in a range of $2\theta = 20°–100°$ was used for capturing the XRD data with a Bruker D8 Advance Da Vinci with a Lynxeye 1D detector.

3. Results and discussion

A backscatter image of the sectioned view of the sandwich structure outlined in Fig. 1(b) is shown in Fig. 2(a). LoF defects are observed in the deposition sequence of IN718 above GRCop-42. Fig. 2(b) is an enlarged view of one of these defects, showing the presence of unmelted powder particles (identified by the dashed yellow arrows), and highlighting the potential for these LoF defects to produce cracks (identified by the solid yellow arrows). The EDS maps of Cu and Ni (Fig. 2(c) and (d) respectively), show the unmelted powder particles to be rich in Ni, and therefore to be IN718. Such defects are also identified in the deposition of IN625 on GRCop-42 using DED [3], and are attributed to the thermal properties of the GRCop-42 substrate. Although the exact temperature of the melt pool is not measured, the thermal conductivity is one order of magnitude greater for GRCop-42 than for IN718, as shown in Table 2. Therefore, melting of the IN718 powder onto the GRCop-42 substrate will result in a melt pool of reduced temperature (compared to deposition onto IN718) due to the higher thermal dissipation from the substrate conductivity. This leads to unmelted powder particles and LoF defects (Fig. 2(b)), along with limited mixing of the alloys (Fig. 2(c) and (d)). Eliminating the porosity defects is critical as they will act as crack initiators under tension or fatigue, increasing the risk of failure at the interface. A simple solution is to increase the laser power for the first few layers of IN718, increasing the temperature of the melt pool to sufficiently melt the powder particles. Evidence of this is presented in the appendix, Figure A 4, with similar results found in the study by Preis et al. [3].

Deposition of GRCop-42 on IN718 does not present defects; instead, a localised change in microstructure occurs between the columnar IN718 and columnar GRCop-42 grains, as evident in Fig. 2(f). The EDS maps of Cu and Ni, (Fig. 2(g) and (h) respectively), shows this deposition order to produce significant mixing across the interface, which corresponds with the region of a localised change in microstructure. Grain refinement occurs within the region of mixing of these alloys, as presented in the corresponding IPF map shown in Fig. 2(i). A closer look at the refined grains, presented in Fig. 2(j), shows evidence of epitaxial grain growth. This is in contrast to the IPF map for IN718 deposited on GRCop-42 (Fig. 2(e)), which has a significant lack of epitaxial grain growth. This grain refinement observed at the interface could be beneficial as it is expected to locally strengthen the interface via Hall-Petch strengthening [26].

The difference in mixing of the alloys due to deposition sequence is explored further with the change in composition across the interface mapped out on backscatter images in Fig. 3(a) and (d) for IN718 on GRCop-42, and GRCop-42 on IN718 respectively. Mixing of the alloys predominantly occurs above the transition line for both deposition sequences, with significantly greater mixing occurring as GRCop-42 is deposited on IN718. This may be explained by the reduced melt pool temperature when depositing IN718 on GRCop-42, which reduces the size of the melt pool (and potentially changes the melting mode) and subsequently limits mixing across the interface. Similar behaviour was observed in a multi-material PBF-LB study involving a copper alloy [22]. The jagged curves of the elements for both deposition sequences (particularly prominent for the deposition of GRCop-42 on IN718, in Fig. 3(d)) indicates the alloys tend to maintain their individual compositions rather than form a new solid solution at the interface. This may suggest a certain degree of immiscibility between these two alloys which could increase crack susceptibility under mechanical loading or thermal cycling [27].

The mixing may result in new phases developing at the interface. To assess this, XRD depth profiling throughout the interface was conducted for IN718 on GRCop-42 and GRCop-42 on IN718, as presented in Fig. 3 (b) and (e) respectively. IN718 and GRCop-42 are both of a predominantly face centred cubic (FCC) crystal structure and have a similar lattice constant (0.362 nm for GRCop-42 [28] and 0.359 nm for IN718

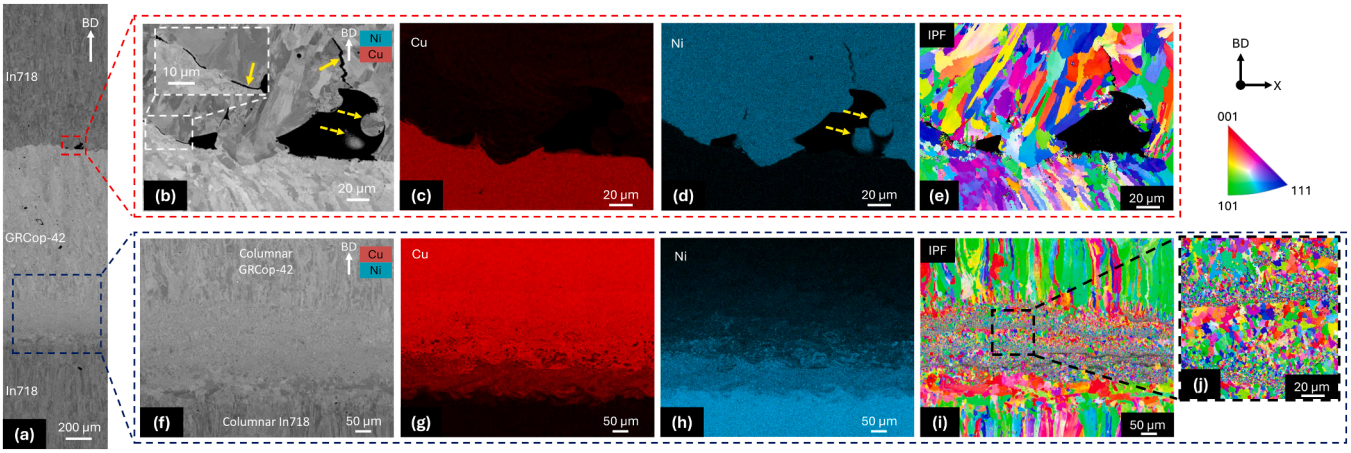

Fig. 2. Horizontal interface of both deposition sequences, reflecting the geometry shown in Fig. 1(b). (a) is a backscatter image covering both interfaces. (b-e) are the backscatter, Cu EDS, Ni EDS, and inverse pole figure (IPF) maps for deposition of IN718 on GRCop-42 respectively. (f-j) are the backscatter, Cu EDS, Ni EDS, and IPF maps for deposition of GRCop-42 on IN718 respectively. The IPF key is shown with the (001) orientation aligned to the BD.

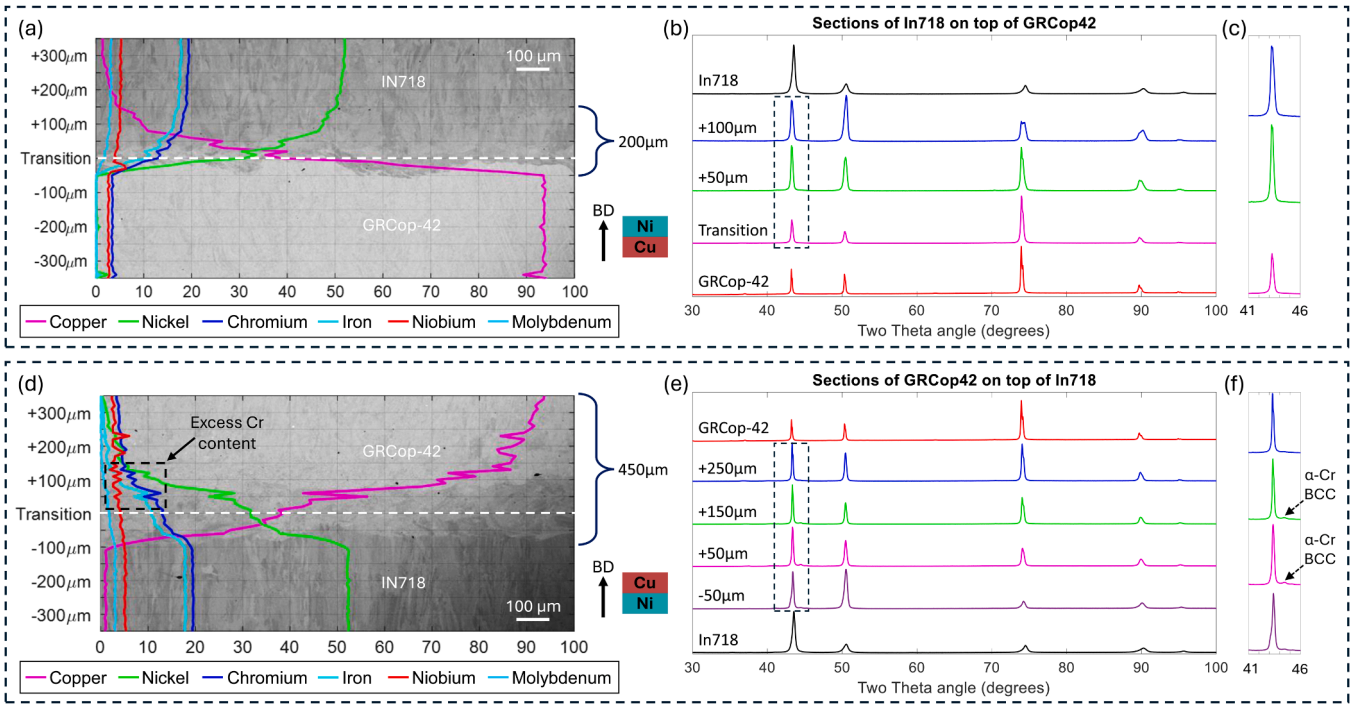

Fig. 3. (a) and (d) are backscatter images of the interface with the average change in composition overlayed for the deposition sequence of IN718 on GRCop-42, and GRCop-42 on IN718 respectively. (b), (c) and (e), (f) display the XRD depth profiling results for the deposition sequence of IN718 on GRCop-42, and GRCop-42 on IN718 respectively.

[29]). Therefore, the intensity peaks are of a relatively similar position for each of the individual alloys. The sections at the different depths of the interface when depositing IN718 on GRCop-42 identify no new phases of a distinct crystal structure (in great enough quantities to be captured using conventional XRD), as outlined by Fig. 3(c). In contrast, the reverse deposition identifies a small additional peak near the interface, at +50 μm and +150 μm above the material transition line (copper rich region of the interface), as highlighted by the dashed black arrows in Fig. 3(f). The position of this new peak correlates with a body centred cubic (BCC) α-Cr phase [30], which is also found to occur in the copper rich region of the interface when depositing GRCop-42 on IN718 using DED (but not in the reverse deposition sequence) [4]. The mixing of the alloys during the deposition of GRCop-42 onto IN718, causes significant levels of Cr (from the IN718) to travel into the GRCop-42 region above the transition line (driven by the Marangoni convection of the melt pool). The high Cr content found in the regions above the transition line, shown by the dashed black box in Fig. 3(d), exceeds the threshold for solubility within the Cu matrix [31] or the Cr_2Nb phase [10] and precipitates as the BCC α-Cr phase. As observed in Fig. 3(a), the Cr content which dilutes into the underlying GRCop-42 does not exceed the Cr level present in the composition of GRCop-42 (indicating limited remelting of the GRCop-42), and therefore the α-Cr phase does not precipitate. In addition to the Cr content, there is migration of a considerable amount of Fe across the interface when depositing GRCop-42 on IN718 (Fig. 3(d)). The presence of Fe in the Cu matrix is known to alter the microstructure, transforming the grains from columnar to equiaxed [32,33]; this effect is evident in Fig. 2(i).

Backscatter images and the corresponding Cu and Ni EDS maps of the geometries presented in Fig. 1(c), (d), and (e) are shown in Fig. 4(a1–6), (c1–6) and (e1–6) respectively. The backscatter images and corresponding Cu and Ni EDS maps of the geometries presented in Fig. 1(f), (g), and (h) are shown in Fig. 4(b1–6), (d1–6), and (f1–6) respectively. By measuring from the edge of the sectioned sample and comparing to the interface position of the build file, the nominal position of the interface is estimated and highlighted by the dashed yellow lines.

The samples with GRCop-42 on IN718 for the angled portion, and with the interface plane perpendicular to the RD, shown in Fig. 4(a1–6) and c(1–6), present similarities in the mixing of the alloys. Crossing of the IN718 (Ni content) across the nominal interface occurs for both to a similar degree, and in a broadly similar manner, particularly for the angled portion of the samples. Hence, indicating that the RD for this sample orientation, with the interface plane perpendicular to the RD, has little effect on the mixing at the interface.

On the other hand, the samples with IN718 on GRCop-42 for the angled portion, and with the interface plane perpendicular to the RD, Fig. 4(b1–6) and (d1–6), present significantly different mixing behaviour. With the RD in the positive x-axis (Fig. 4(b1–6)), there is a well-defined boundary between the alloys, with minimal evidence of the Ni or Cu content crossing over the interface. Recoating in the negative x-axis (Fig. 4(d1–6)) produces waves of Ni crossing into the GRCop-42 region, in a pattern reflecting the Marangoni flow of the melt pool and at a frequency identical to the layer height, outlined by the dashed white curves in Fig. 4(d2) and (d5). The sample shown in Fig. 4(b1–6) reveals the presence of porosity defects (highlighted by the dashed white arrows).

The powder deposition mechanism can impact the mixing of the alloys, with over-deposition of powder or insufficient suction from the leveller causing significant amounts of one material to cross over the nominal interface. The effects of these parameters are exacerbated by the RD (and recoating speed), therefore they are more prominent when the interface plane is perpendicular to the RD. Insufficient suction from the leveller will cause powder to build up at the edge of the levelling blade and smear across the interface, in the RD; this would result in mixing which is shown in Fig. 4(c1–6). However, as shown in Fig. 4 (a1–6) and (d1–6), the mixing of the alloys across the nominal interface is in the reverse of the RD and is therefore not as a result of the smearing of the powder due to insufficient suction. Therefore, insufficient suction from the leveller is not the cause for the mixing behaviour across the interface.

Fig. 5 displays schematics of the process by which multiple materials are deposited using the Schaeffler Aerosint SPD recoater. Fig. 5(a) displays an “ideal” scenario, in which the powder falls vertically

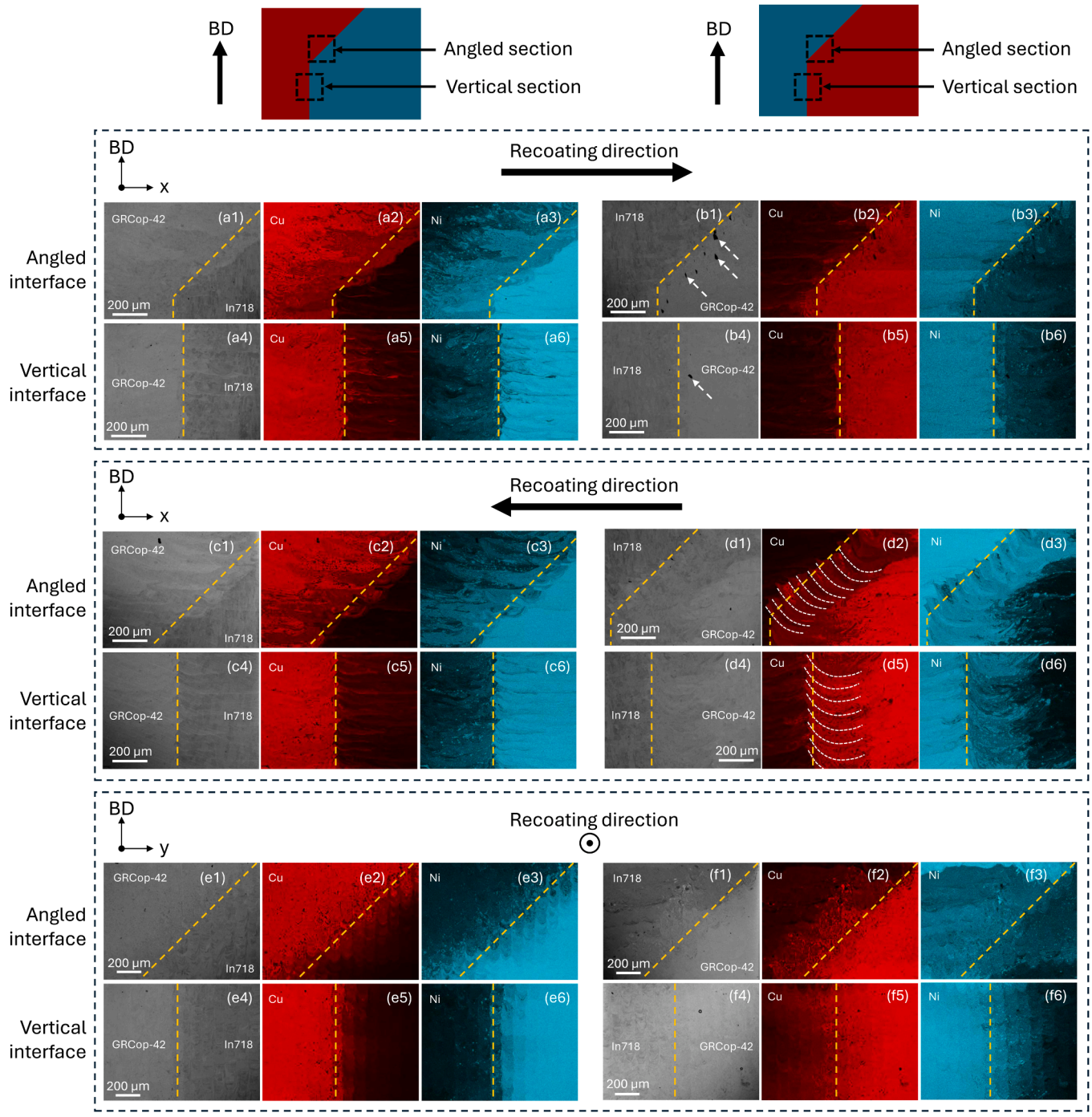

Fig. 4. (a1–6), (c1–6), and (e1–6) are the backscatter images, Cu EDS maps, and Ni EDS maps for the geometries presented in Fig. 1(c), (d), and (e) respectively. (b1–6), (d1–6), and (f1–6) are the backscatter images, Cu EDS maps, and Ni EDS maps for the geometries presented in Fig. 1(f), (g), and (h) respectively. The nominal position of the interface is highlighted by the dashed yellow lines.

downwards (from only gravity) onto the build plate. In reality, due to the ejection pressure, the particles are forcefully ejected from the curved surface of the mesh and fall at a slight angle towards the build plate. This is reflected in Fig. 5(b), and results in the first material deposited crossing over the nominal interface. As previously shown in Fig. 1(a), for this sequence of experiments, deposition of IN718 occurs first; as such, if there is any overlap of the materials at the interface the underlying IN718 of the layer will remain, whilst the upper layer of GRCop-42 will be removed by the levelling blade. This would explain the significant presence of Ni in the GRCop-42 region of the interface shown in Fig. 4 (a1–6), (c1–6) and (d1–6). On the other hand, Fig. 4(b1–6) presents a well-defined boundary, but also contains porosity defects at the interface. This suggests that this sample may not have been receiving enough powder (a symptom of the deposition mechanism) to create a significant overlap of materials at the interface. This scenario is presented in Fig. 5 (c) where there is insufficient powder at the interface, producing porosity defects, but also limiting the amount of the first deposited material which crosses over the nominal interface.

The porosity visible in Fig. 4(b1–6) occurs on the opposite side of the interface to that seen for the horizontal interface of IN718 on GRCop-42 in Fig. 2(b). This stems from different formation mechanisms. For the horizontal IN718 on GRCop-42 interface (Fig. 2(b)), the pores in the

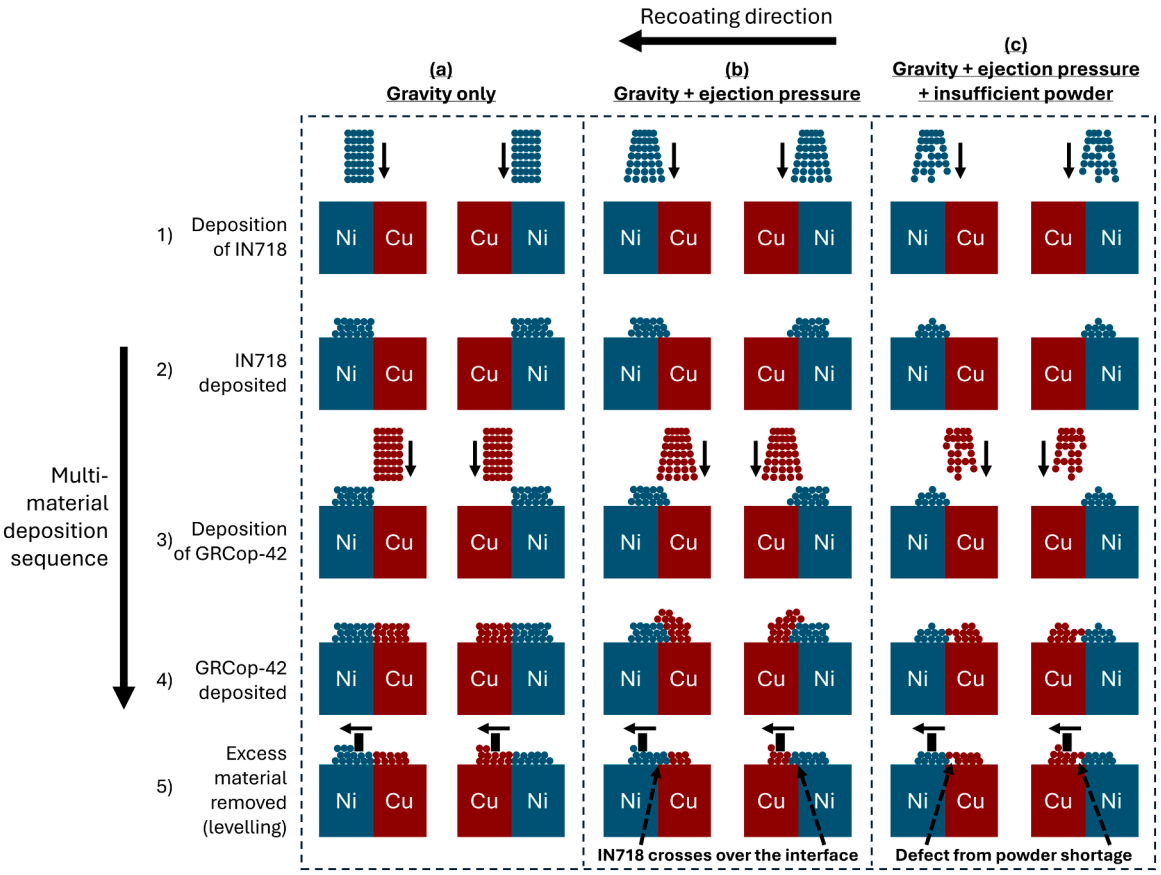

Fig. 5. Schematics of the powder deposition for a multi-material layer under different powder ejection scenarios. (a) presents a multi-material layer when under "ideal" conditions where powder falls due to gravity only. (b) is the scenario in which ejection pressure is used to force powder off the drums, leading to IN718 crossing over the interface. (c) presents the scenario of ejection pressure depositing an insufficient amount of powder on to the substrate, which can result in porosity defects and reduced crossing of IN718 over the interface.

IN718 are LoF defects driven by laser energy input and melt pool instability on a highly conductive Cu-alloy substrate. This mechanism allows for the pores to be removed through increased laser power, as observed in Figure A 4. In contrast, the porosity observed in the GRCop-42 region of the vertical/angled interface (Fig. 4(b1–6)) is an artefact arising from the powder deposition process (local short-feeding of powder as illustrated in Fig. 5(c)), rather than melt pool instability.

Deposition of the GRCop-42 on IN718 samples with the vertical interface plane parallel to the RD is presented in Fig. 4(e1–6). This sample orientation presents significantly different mixing behaviour from those shown in Fig. 4(a1–6) and (c1–6), with the melt pools clearly reflected in the regions near the interface in the EDS maps of Cu and Ni. The gradual transition across the interface in Cu and Ni content provides a compositional gradient effect for the angled and vertical interfaces. This gradual change in composition may be beneficial for alleviating stresses which develop at the interface due to a mismatch in the physical or thermal properties of the two alloys (during operation of the bimetallic structure) [11]. Similar differences in the transition of material across a vertically aligned interface were also observed with the deposition of the M300 tool steel (BCC) and CuCrZr (FCC) using a Schaeffler Aerosint SPD recoater [34]. As such, the findings of this study can be useful when considering the interface of other bimetallic systems.

The opposite deposition sequence for this sample orientation is presented in Fig. 4(f1–6). The vertical section of this sample (Fig. 4(f4–6)) presents a similar compositional gradient effect to that shown in Fig. 4(e4–6), but over a greater distance in the y-axis, whereas the angled portion of the sample does not present similar behaviour. Rather, there are significant quantities of Ni in the GRCop-42 region of the nominal interface (Fig. 4(f3)) which do not represent melt pool dynamics or the recoating pattern. As discussed, in relation to the samples shown in Fig. 4(a1–6), (c1–6) and (d1–6), the other samples from this build present evidence of excessive ejection pressure for the IN718. Due to the nature of the deposition recoater, different sections of the build plate may also be exposed to higher ejection pressure (and therefore an increased amount of IN718 at the nominal interface) than others. It is possible the sample presented in Fig. 4(f1–6) was located in a region on the build plate which correlated with extreme levels of ejection pressure from the drum containing IN718 powder. Therefore, as the recoater passed over this section of the build plate, an excess of IN718 particles was ejected from the drum and fell in the GRCop-42 region of the sample. Regardless of the poor accuracy of deposition for some of the samples presented in Fig. 4, the interface is shown to be defect-free.

The samples in Fig. 4, provide different behaviours in the mixing of the alloys across the interface. Three of these distinct behaviours – crossing of Ni content across the nominal interface (Fig. 4(a1–6)), a well-defined boundary with little mixing/crossing of the alloys (Fig. 4(b1–6)), and the compositional gradient effect achieved (Fig. 4(e1–6)) – are studied in greater detail to elucidate their effect on the microstructure at the interface. The microstructure of the transition point between the vertically aligned and angled portion of the samples, along with the corresponding EDS maps for Cu and Ni, are presented in Fig. 6.

Fig. 6(a1–3) displays the sample with the crossing of Ni (IN718) across the interface. As is also observed in Fig. 2(i) and (j), the mixing across the interface has a grain refinement effect. The enlarged view of a region of grain refinement is presented in Fig. 6(d1–3), indicating the evolution of equiaxed grains, with finer grains located in the Cu-rich regions and coarser grains in the Ni-rich regions. The samples which present a well-defined boundary, Fig. 6(b1–3), and the compositional

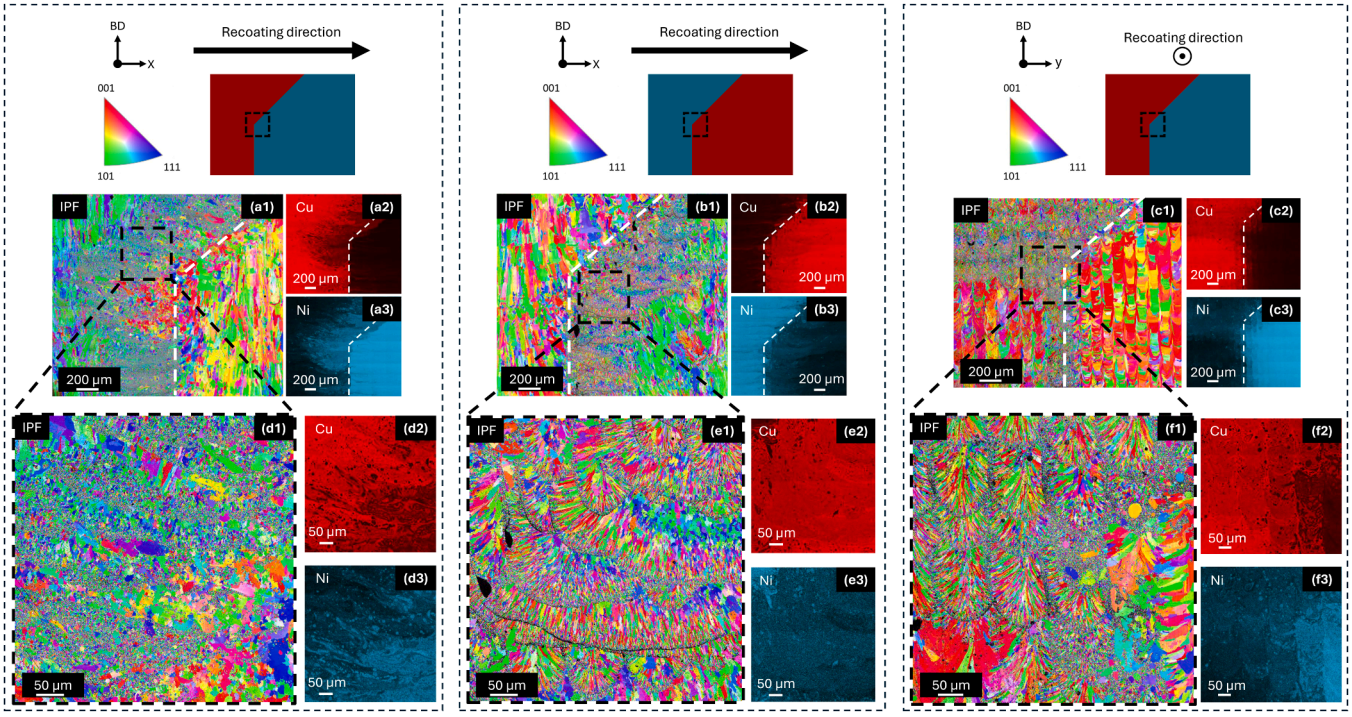

Fig. 6. Microstructure of the interface covering the vertical and angled sections of three samples from Fig. 4. (a1–3), (b1–3), and (c1–3) are the IPF, Cu EDS maps, and Ni EDS maps for the samples shown in Fig. 4 (a1–6), (b1–6), and (e1–6) respectively. (d1–3), (e1–3), and (f1–3) are the IPF and corresponding EDS maps for the refined grain regions shown in (a1–3), (b1–3), and (c1–3) respectively. The recoater deposits parallel to the x-axis. The IPF key is shown with the (001) orientation aligned to the BD. The nominal position of the interface is highlighted by the dashed white lines.

gradient effect, Fig. 6(c1–3), also reflect the grain refinement to predominantly occur where there is Ni contamination in the Cu matrix. The enlarged view of the regions of grain refinement for these samples are presented in Fig. 6(e1–3) and (f1–3), respectively. Both present two distinct grain morphologies in the Cu-rich areas; either fine, equiaxed grains or columnar dendrites, reflecting the morphology of the melt pools. Additionally, the Ni-rich regions of the mixing area produce fine equiaxed grains, but of a coarser form than those observed in the Cu-rich regions. The formation of fine equiaxed grains in the Cu matrix is potentially due to the heterogeneous nucleation effect of the Fe-rich regions (from the IN718) in the Cu alloy [33], whereas the grain refinement effect on the Ni-rich regions is likely driven by the increased cooling rate due to the proximity with the high thermal conductivity of the Cu alloy.

The differences in interfacial microstructure, from the various interface alignments, are likely to influence the mechanical and thermal response of the bimetallic structure. The grain refinement observed at the interface across all samples presented in Fig. 6 is likely to raise the local yield strength, via the Hall-Petch relationship [26], improving the resistance of the interface to local yielding. In the case where the RD is parallel to the interface plane, the graded chemical transition (Fig. 4 (e1–6), Fig. 6(c1–3) and Fig. 6(f1–3)) could also provide a smoother change in the thermophysical properties between IN718 and GRCop-42 (Table 2). This would help to alleviate thermal stresses at the interface, and ultimately, be beneficial for thermal fatigue resistance under cyclic loading.

4. Conclusion

A detailed understanding of the microstructure evolution at the interface of combined IN718 and GRCop-42, and how it is influenced by the interface orientation is critical to enable confidence in the operation of these bimetallic structures. This study has shown that the orientation of the interface relative to both the BD and the RD has a significant effect on the formation of defects and the microstructure evolution at the interface. A summary of the key insights from this study are listed below:

- For a horizontal interface, there are key differences based on the deposition sequence. LoF defects develop at the interface when depositing IN718 on GRCop-42 due to the high thermal conductivity of the substrate material, with unmelted IN718 particles present. On the other hand, the precipitation of the BCC α-Cr phase and grain refinement occurs at the interface when depositing GRCop-42 on IN718 due to significant mixing of the alloys.
- For vertical and angled interfaces, the interface is affected by the RD and is sensitive to the deposition parameters. Significant crossing of the first deposited material into the second occurs when the interface plane is perpendicular to the RD. Whereas, when the interface plane is parallel to the RD, a graded transition of the alloys across the interface is achieved. The difference in mixing of the alloys due to the interface alignment (relative to the RD) may therefore have an influence on the development of defects (such as cracks) during thermal cycles. Hence, when producing samples with a non-horizontal interface, the part orientation and deposition order will have a significant effect on the interface morphology and potentially affect the mechanical properties.
- The change in the microstructure evolution at the interface is impacted by the mixing of the alloys. With samples where there is significant crossing of IN718 across the nominal interface, columnar to equiaxed transformation of the grains occurs, with finer grains located in the Cu-rich regions and coarser grains located in the Ni-rich regions of the interface. On the other hand, samples with a sharp transition at the interface, result in columnar dendritic growth in the Cu-rich regions. This difference may impact the mechanical performance of the bimetallic structure.
- The mixing of the alloys at the interface is shown to be largely dependent on the deposition mechanism for the vertical and angled interfaces in this study. Porosity and contamination across the

interface are evident and governed by the quality and consistency of the recoating process. Therefore, considerable effort should be made to understand and optimise the deposition process for future experiments.

This study has shown it is feasible to produce defect-free bimetallic structures of IN718 and GRCop-42 using PBF-LB. However, of note, there are clear differences in the microstructure evolution based on the orientation of the interface, relative to both the BD and the RD, of which the effect on the mechanical properties is not known. Therefore, future work will focus on mechanical testing – particularly tensile and fatigue testing – to quantify and observe the effect of interface orientation on the deformation and failure mechanisms of these bimetallic structures.

CRediT authorship contribution statement

Alasdair Bulloch: Writing – original draft, Visualization, Methodology, Investigation, Conceptualization. **Amanda Cruchley:** Writing – review & editing, Supervision, Methodology. **Allin Groom:** Writing – review & editing, Supervision, Methodology. **Andy Harris:** Writing – review & editing, Supervision, Methodology. **Fiona Schulz:** Writing – review & editing, Supervision, Methodology. **Christopher J. Tuck:** Writing – review & editing, Supervision, Resources, Funding acquisition. **Richard Hague:** Writing – review & editing, Supervision, Resources, Funding acquisition, Conceptualization. **Marco Simonelli:** Writing – review & editing, Supervision, Resources, Methodology, Investigation, Conceptualization.

Declaration of competing interest

The authors declare the following financial interests/personal relationships which may be considered as potential competing interests:

Alasdair Bulloch reports financial support was provided by Autodesk Inc. Alasdair Bulloch reports financial support was provided by The Manufacturing Technology Centre Limited. If there are other authors, they declare that they have no known competing financial interests or personal relationships that could have appeared to influence the work reported in this paper.

Acknowledgements

The work was supported by the Engineering and Physical Sciences Research Council [grant numbers EP/P031684/1 and EP/V029010/1], Autodesk Research (London, UK), and The Manufacturing Technology Centre (Coventry, UK). The authors would like to thank the Centre for Additive Manufacturing (CfAM) lab and the Materials lab in Wolfson Building for access to laboratory equipment. The authors also thank the Nanoscale and Microscale Research Centre (nmRC) for providing access to analytical instrumentation and acknowledge Dr Nigel Neate for assistance with EBSD.

Appendix

Fig. A.1, Fig. A.2, Fig. A.3, Fig. A.4

1.1. Powder properties

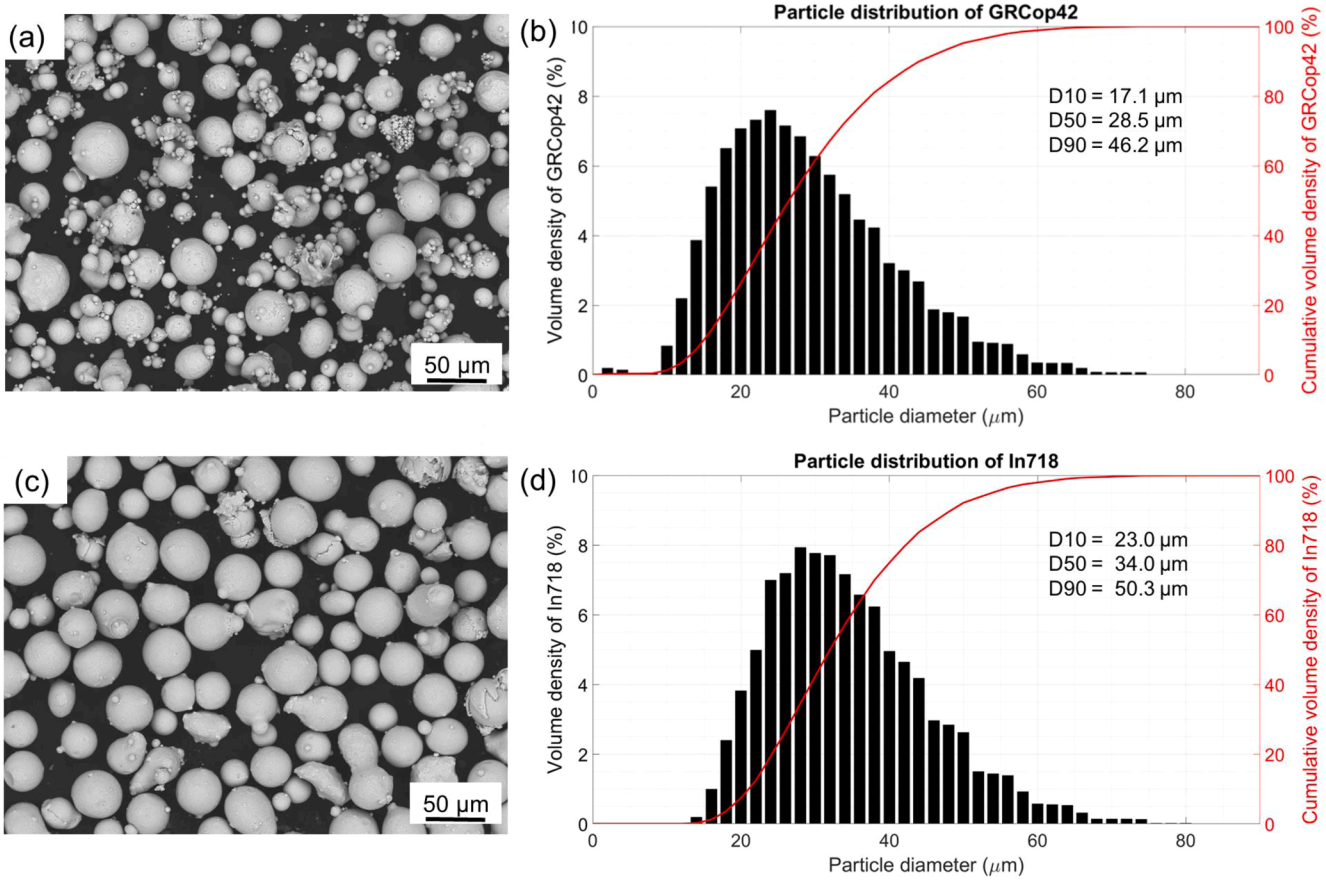

Fig. A.1. Characterization of the powder used in this study, (a) Scanning electron microscope (SEM) image showing the morphology of the GRCop-42 powder, (b) particle size distribution of the GRCop-42 powder, (c) SEM image of the IN718 powder, and (d) particle size distribution of the IN718 powder.

1.2. Sample dimensions

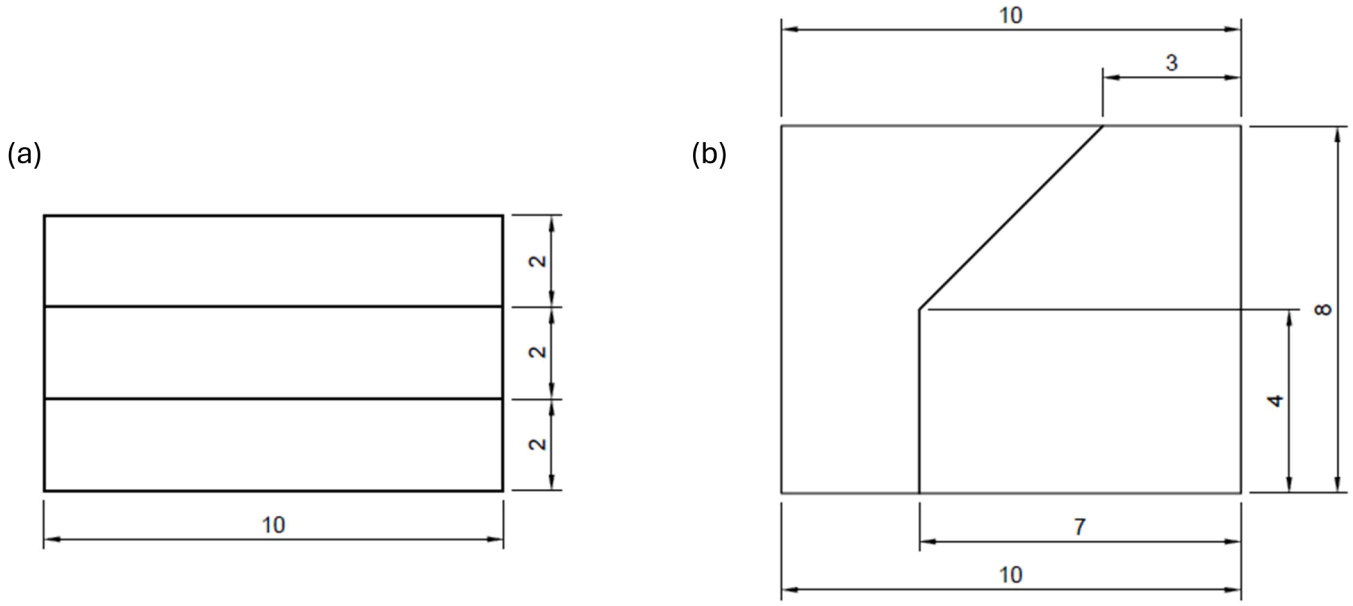

Fig. A.2. Dimensions (in mm) of the samples produced in this study. (a) is of the sandwich structure with the horizontal interfaces, and (b) is the sample with the vertical and angled interface.

1.3. EDS linescan methodology

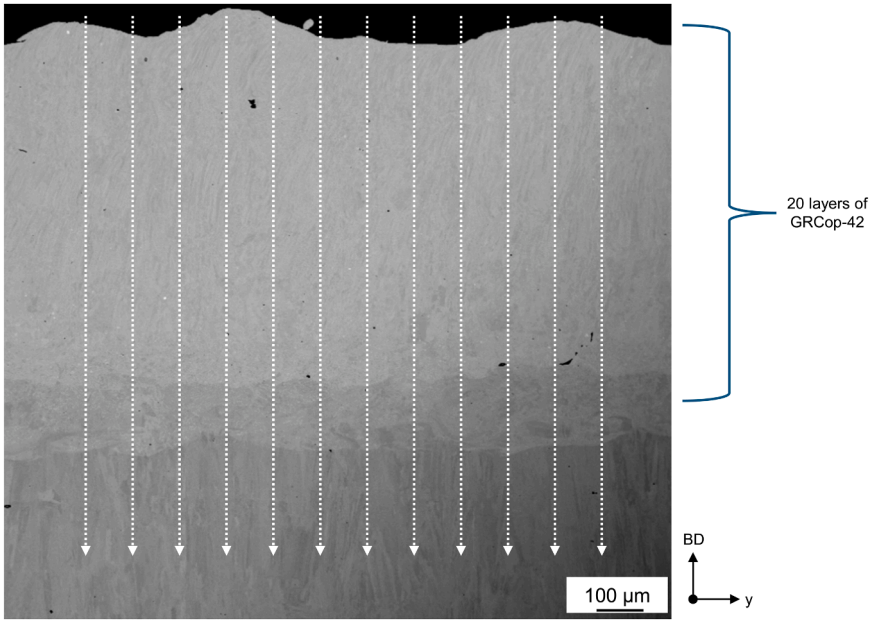

Fig. A.3. EDS linescan methodology across the interface of GRCop-42 on IN718. Each dashed white arrow represents a scan line which records a local chemical composition every ten microns along the scan line.

1.4. Effect of laser power on horizontal interface of IN718 on GRCop-42

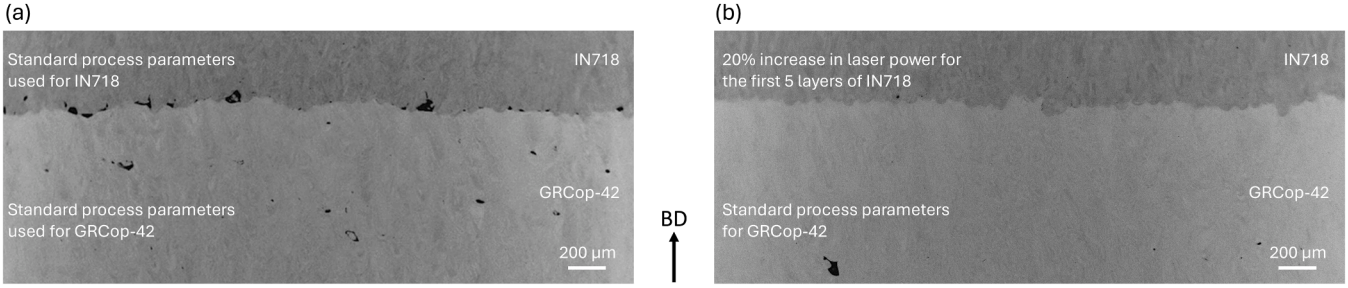

Fig. A.4. Effect of laser power on LoF defects at the interface of IN718 deposited on GRCop-42. (a) Use of optimised parameters (200 W) developed for IN718, (b) increased laser power by 20 % (240 W) for the first five layers of IN718 deposited on GRCop-42.

Data availability

Data will be made available on request.

References

[1] M. Schneck, M. Horn, M. Schmitt, C. Seidel, G. Schlick, G. Reinhart, Review on additive hybrid- and multi-material-manufacturing of metals by powder bed fusion: state of technology and development potential, Progr. Addit. Manuf. 6 (2021) 881–894, https://doi.org/10.1007/s40964-021-00205-2.

[2] C. Wei, L. Li, Recent progress and scientific challenges in multi-material additive manufacturing via laser-based powder bed fusion, Virtual. Phys. Prototyp. 16 (2021) 347–371, https://doi.org/10.1080/17452759.2021.1928520.

[3] J. Preis, Z. Wang, J. Howard, Y. Lu, N. Wannenmacher, S. Shen, B.K. Paul, S. Pasebani, Effect of laser power and deposition sequence on microstructure of GRCop42 - Inconel 625 joints fabricated using laser directed energy deposition, Mater. Des. 241 (2024), https://doi.org/10.1016/j.matdes.2024.112944.

[4] A.D. Iams, T.J. Lienert, D.A. Otazu, M. Ramoni, Effects of deposition sequence on microstructural evolution in additively manufactured Cu-Cr-Nb alloy /superalloy bimetallic structures, Addit. Manuf. Lett. 6 (2023), https://doi.org/10.1016/j.addlet.2023.100151.

[5] B.K. Jasthi, T.S. Kuca, M.D. Ellingsen, D.L. Ellis, V.A.S. Kandadai, T.R. Curtis, Microstructure and mechanical properties of cold spray additive manufactured Cu-Cr-Nb and Fe-Ni-Cr alloys, Addit. Manuf. 61 (2023), https://doi.org/10.1016/j.addma.2022.103354.

[6] G.M. Volpato, U. Tetzlaff, M.C. Fredel, A comprehensive literature review on laser powder bed fusion of Inconel superalloys, Addit. Manuf. 55 (2022), https://doi.org/10.1016/j.addma.2022.102871.

[7] G. Demeneghi, B. Barnes, P. Gradl, D. Ellis, J.R. Mayeur, K. Hazeli, Directed energy deposition GRCop-42 copper alloy: characterization and size effects, Mater. Des. 222 (2022), https://doi.org/10.1016/j.matdes.2022.111035.

[8] R.P. Minneci, E.A. Lass, J.R. Bunn, H. Choo, C.J. Rawn, Copper-based alloys for structural high-heat-flux applications: a review of development, properties, and performance of Cu-rich Cu–Cr–Nb alloys, Int. Mater. Rev. 66 (2021) 394–425, https://doi.org/10.1080/09506608.2020.1821485.

[9] A.R. Kini, D. Maischner, A. Weisheit, D. Ponge, B. Gault, E.A. Jägle, D. Raabe, In-situ synthesis via laser metal deposition of a lean Cu–3.4Cr–0.6Nb (at%) conductive alloy hardened by Cr nano-scale precipitates and by laves phase micro-particles, Acta Mater. 197 (2020) 330–340, https://doi.org/10.1016/j.actamat.2020.07.035.

[10] Y. Chen, C. Zeng, H. Ding, S. Emanet, P.R. Gradl, D.L. Ellis, S. Guo, Thermophysical properties of additively manufactured (AM) GRCop-42 and GRCop-84, Mater. Today Commun. 36 (2023), https://doi.org/10.1016/j.mtcomm.2023.106665.

[11] L. Liu, D. Wang, T. Wang, C. Han, Y. Li, H. Tan, W. Zhou, X. Yan, L. Lei, Y. Yang, Laser additive manufacturing of multimaterials with hierarchical interlocking interface via a flexible scraper-based method, Int. J. Mach. Tools. Manuf. 205 (2025), https://doi.org/10.1016/j.ijmachtools.2024.104236.

[12] C. Wei, L. Li, X. Zhang, Y.H. Chueh, 3D printing of multiple metallic materials via modified selective laser melting, CIRP Ann. 67 (2018) 245–248, https://doi.org/10.1016/j.cirp.2018.04.096.

[13] B. Neirinck, X. Li, M. Hick, Powder deposition systems used in Powder bed-based multimetal additive manufacturing, Acc. Mater. Res. 2 (2021) 387–393, https://doi.org/10.1021/accountsmr.1c00030.

[14] C. Wei, H. Gu, Q. Li, Z. Sun, Y. hui Chueh, Z. Liu, L. Li, Understanding of process and material behaviours in additive manufacturing of Invar36/Cu10Sn multiple material components via laser-based powder bed fusion, Addit. Manuf. 37 (2021), https://doi.org/10.1016/j.addma.2020.101683.

[15] D. Herzog, K. Asami, C. Scholl, C. Ohle, C. Emmelmann, A. Sharma, N. Markovic, A. Harris, Design guidelines for laser powder bed fusion in Inconel 718, J. Laser Appl. 34 (2022) 012015, https://doi.org/10.2351/7.0000508.

[16] L. Chechik, I. Todd, Inconel 718 two ways: powder bed fusion vs. directed energy deposition, Addit. Manuf. Lett. 6 (2023), https://doi.org/10.1016/j.addlet.2023.100145.

[17] A.H. Seltzman, S.J. Wukitch, Precipitate size in GRCop-42 and GRCop-84 Cu-Cr-Nb alloy gas atomized powder and L-PBF additive manufactured material, Fusion Sci. Technol. 79 (2023) 503–516, https://doi.org/10.1080/15361055.2022.2147765.

[18] G. Demeneghi, P. Gradl, J.R. Mayeur, K. Hazeli, GRCop-42: comparison between laser powder bed fusion and laser powder direct energy deposition, Addit. Manuf. Lett. 10 (2024), https://doi.org/10.1016/j.addlet.2024.100224.

[19] B. Onuike, B. Heer, A. Bandyopadhyay, Additive manufacturing of Inconel 718—Copper alloy bimetallic structure using laser engineered net shaping (LENS^{TM}), Addit. Manuf. 21 (2018) 133–140, https://doi.org/10.1016/j.addma.2018.02.007.

[20] B. Onuike, A. Bandyopadhyay, Bond strength measurement for additively manufactured Inconel 718- GRCop84 copper alloy bimetallic joints, Addit. Manuf. 27 (2019) 576–585, https://doi.org/10.1016/j.addma.2019.04.003.

[21] T. Pan, X. Zhang, T. Yamazaki, A. Sutton, W. Cui, L. Li, F. Liou, Characteristics of Inconel 625—Copper bimetallic structure fabricated by directed energy deposition, Int. J. Adv. Manuf. Technol. 109 (2020) 1261–1274, https://doi.org/10.1007/s00170-020-05713-z.

[22] A. Bulloch, A. Harris, A. Groom, A. Cruchley, C.J. Tuck, M. Simonelli, Fundamental investigation of the interface formation of multi-material additive manufactured 316L-CuSn10 structures, Metallurg. Mater. Trans. A (2025), https://doi.org/10.1007/s11661-025-07817-1.

[23] T. Huynh, A. Mehta, K. Graydon, J. Woo, S. Park, H. Hyer, L. Zhou, D.D. Imholte, N.E. Woolstenhulme, D.M. Wachs, Y. Sohn, Microstructural development in inconel 718 nickel-based superalloy additively manufactured by laser powder bed fusion, Metallogr., Microstruct., Anal. 11 (2022) 88–107, https://doi.org/10.1007/s13632-021-00811-0.

[24] A.S. Hakeem, F. Patel, N. Minhas, A. Malkawi, Z. Aleid, M.A. Ehsan, H. Sharrofna, A. Al Ghanim, Comparative evaluation of thermal and mechanical properties of nickel alloy 718 prepared using selective laser melting, spark plasma sintering, and casting methods, J. Mater. Res. Technol. 12 (2021) 870–881, https://doi.org/10.1016/j.jmrt.2021.03.043.

[25] D. Deng, R.L. Peng, H. Brodin, J. Moverare, Microstructure and mechanical properties of Inconel 718 produced by selective laser melting: sample orientation dependence and effects of post heat treatments, Mater. Sci. Eng.: A 713 (2018) 294–306, https://doi.org/10.1016/j.msea.2017.12.043.

[26] T. DebRoy, H.L. Wei, J.S. Zuback, T. Mukherjee, J.W. Elmer, J.O. Milewski, A. M. Beese, A. Wilson-Heid, A. De, W. Zhang, Additive manufacturing of metallic components – Process, structure and properties, Prog. Mater. Sci. 92 (2018) 112–224, https://doi.org/10.1016/j.pmatsci.2017.10.001.

[27] J. Preis, D. Xu, B.K. Paul, P.A. Eschbach, S. Pasebani, Effect of liquid miscibility gap on defects in Inconel 625–GRCop42 joints through analysis of gradient composition microstructure, J. Manuf. Mater. Process. 8 (2024), https://doi.org/10.3390/jmmp8010042.

[28] D.L. Ellis, G.M. Michal, Mechanical and thermal properties of two Cu-Cr-Nb alloys and NARloy-Z, 1996. https://ntrs.nasa.gov/citations/19970002915.

[29] R.M. Nunes, D. Pereira, T. Clarke, T.K. Hirsch, Delta phase characterization in Inconel 718 alloys through x-ray diffraction, ISIJ Int. 55 (2015) 2450–2454, https://doi.org/10.2355/isijinternational.ISIJINT-2015-111.

[30] X. Xie, G. Wang, J. Dong, C. Wu, J. Radavich, G. Shen, B. Lindsley, Alpha chromium formation in alloy 718 and its effect on creep crack propagation, 2001. https://doi.org/10.7449/2001/Superalloys_2001_399_410.

[31] Q. Mao, Y. Liu, Y. Zhao, A review on copper alloys with high strength and high electrical conductivity, J. Alloys. Compd. 990 (2024), https://doi.org/10.1016/j.jallcom.2024.174456.

[32] B. Li, H. Zhang, J. Cui, Effect of cooling rate and iron content on the solidification structures of copper-iron alloys, Adv. Mat. Res. (2011) 89–93, https://doi.org/10.4028/www.scientific.net/AMR.327.89.

[33] Y. Liu, J. Zhang, Q. Sun, M. Li, M. Yan, X. Cheng, M. Li, M.X. Zhang, Laser powder bed fusion of copper matrix iron particle reinforced nanocomposite with high strength and high conductivity, J. Mater. Sci. Technol. 134 (2023) 50–59, https://doi.org/10.1016/j.jmst.2022.06.007.

[34] X. Li, Z. Pan, L. Smolej, V. Karthik Nadimpalli, M. Moshiri, Towards manufacturing intra-layer multi-material mould tools with vertical interfaces using laser-based powder bed fusion, Mater. Des. 243 (2024), https://doi.org/10.1016/j.matdes.2024.113056.